



Research article

Experimental investigation and comparison of PBI/MWCNT and PSF/MWCNT membranes for recovering water from RO reject of brackish water by FO

Sharan Srinivas Venkatesh^{a,*}, Pandiyarajan Vellaichamy^a,
Sundararajan Thirumalachari^b, Velraj Ramalingam^c, Mohan Doraiswamy Raju^a

^a Department of Chemical Engineering, AC Tech, Anna University, Chennai, 600 025, Tamil Nadu, India

^b Department of Mechanical Engineering, Indian Institute of Technology Madras, Chennai, 600 036, Tamil Nadu, India

^c Institute for Energy Studies, Anna University, Chennai, 600 025, Tamil Nadu, India

ARTICLE INFO

Keywords:

Polybenzimidazole
Polysulfone
Multi-walled carbon nanotubes
Membranes
Forward osmosis

ABSTRACT

The performances of polybenzimidazole (PBI) and polysulfone (PSF) membranes for recovering water from reverse osmosis (RO) reject of brackish water through forward osmosis (FO) were assessed and compared. Non-functionalised multi-walled carbon nanotubes (MWCNT) were added to the membrane casting solutions, with concentrations ranging from 0 to 3 wt%. The experiment was conducted for eight samples using RO reject of brackish water as the feed solution (FS) and 2 M analytical grade MgCl₂ as the draw solution (DS). The hydrophilicity, water permeability, salt rejection rate (R_s), water flux (WF) and porosity of the membranes improved with increasing MWCNT content up to 2 wt%. Also, the structural parameter, salt permeability and reverse solute flux decreased. PBI/MWCNT_{2 wt%} exhibited the best performance among the membranes tested compared with porosity of 70 ± 4 %, structural parameter of 0.36 ± 0.2 μm, and R_s of 93.5 %. In contrast with the pristine PBI membrane, an average water flux enhancement of 15 % and 49 % was observed for the FS and DS sides, respectively, for PBI/MWCNT_{2 wt%}. It is evident from the results that including MWCNT improves the performance of both membranes, with better relative performance for PBI membranes than PSF membranes.

1. Introduction

Water scarcity and contamination threaten life globally, affecting quality of life and industrial growth. By 2030, water consumption is anticipated to increase by 53% to 6.9 trillion m³ [1–3]. Among the present water treatment technologies, membrane-based processes like nanofiltration (NF), reverse osmosis (RO), multi-stage flash evaporation (MSF), ultrafiltration (UF) and multi-effects distillation (MED) are widely implemented to mitigate water scarcity by producing clean and potable water [4,5].

Forward osmosis (FO) technology is a rapidly developing method of treating and recovering water where it is separated from dissolved solutes using a semi-permeable membrane and osmotic pressure as the natural driving potential. The dissolved solutes are retained, and water alone is carried across the membrane due to differences in osmotic pressure. FO process uses a draw solution (DS) having an osmotic pressure higher than the feed solution (FS). FO consumes less pumping energy while also producing good product

* Corresponding author.

E-mail address: aruna1572@gmail.com (S.S. Venkatesh).

quality. Additionally, it has a low fouling rate compared to contemporary methods [6–10]. It also has a high percentage of water recovery and a low carbon footprint [11,12]. Due to these relative advantages, FO has the potential to be an attractive water recovery technology, especially for removing organic contaminants and toxic heavy metal impurities [9,10]. However, the need to produce more high-quality membranes, an ideal DS and mitigation of internal concentration polarisation (ICP) poses challenges for FO [10,11,13].

An ideal DS is essential for FO since it provides the osmotic pressure difference needed for transporting water across the membrane. Besides high osmotic pressure difference, an ideal DS should promote high water flux (WF) and low viscosity for easy flow and low ICP. The DS must be relatively inexpensive, abundant, and easily recoverable after application in FO [14]. Many inorganic DS are implemented due to their advantages of being affordable, plentiful, compatible with most FS, and having low toxicity and high osmotic pressure. All these advantages assist in mitigating ICP [14,15]. $MgCl_2$ has been used as DS for FO membranes as an alternative to other commonly used NaCl, KBr, KCl, $CaSO_4$ and $MgSO_4$ solutions. This is because $MgCl_2$ is a divalent salt with a low diffusion coefficient in water (thereby reducing ICP) and has high osmotic pressure, which increases WF [14,16–18]. In addition, $MgCl_2$ can be easily recovered via NF [19].

Proper membrane design is crucial for its performance and efficiency. FO membranes should be chemically, thermally, and mechanically stable and have high WF, low fouling tendency, low ICP and low reverse solute flux (RSF) [5]. Making the membrane support layer more hydrophilic and minimising the structural parameter (S) contributes to mitigating ICP further [6,20–23]. Therefore, manufacturing membranes that provide a high salt rejection rate and WF is essential [16,17,24]. Thin-film composite as well as thin-film nanocomposite (TFC and TFN, respectively) membranes are predominantly used in FO because of their excellent permeability and selectivity [25]. TFC membranes are comprised of an active layer stacked above a support layer since they can independently enhance the performance of the support layer while offering favourable separation capabilities across a wide range of operating temperatures and pH [15,25,26]. TFN membranes, on the other hand, are formed when nanoparticles are incorporated into TFC membranes. This also helps improve the membrane solute rejection performance, preventing minuscule-sized contaminants from passing through the membrane [25]. Techniques such as interfacial polymerisation (IP) and phase inversion (PI) are the ones usually implemented for making TFC and TFN membranes for FO [25–28]. Recently, the incorporation of nanomaterials like multi-walled carbon nanotubes (MWCNT) and graphene oxide (GO), and metals/metal oxides like zeolites, gold (Au), copper (Cu), aluminium oxide (Al_2O_3), silica (SiO_2), zinc oxide (ZnO), iron (III) oxide (Fe_3O_4) and titanium dioxide (TiO_2) were carried out in TFN membranes. These nanoparticles mitigate limitations concerning WF and fouling and improve membrane hydrophilicity, permeability, stability, and selectivity. Nanoparticles also help reduce risks affiliated with radioactive contaminants and enhance water molecule transport and the mechanical properties of the membranes [4,5,16,28–32].

MWCNT nanoparticles exhibit excellent stability and improved thermal properties for enhanced water transport across the membrane. By embedding MWCNT in the active layer of thin film membranes, the antifouling capabilities, WF and salt rejection rates can be enhanced [16,20,25,29]. Polymeric materials, such as polybenzimidazole (PBI) and polysulfone (PSF), exhibit good potential for TFC and TFN FO membranes. Due to its aromatic heterocyclic molecular structure, PBI exhibits remarkable chemical properties, such as forming intramolecular and intermolecular hydrogen bonds with neighbouring PBI molecules. In aqueous environments, PBI becomes self-charged. It also has high thermal (resistance at high temperatures) stability, mechanical (high tensile strength) stability, and high pH tolerance (2–14), and it is less prone to fouling. PSF is usually implemented as a polymer substrate for preparing membranes to promote better chemical, thermal, and mechanical stability; it also accommodates greater pH tolerance (2–13). Membranes with high concentrations of PSF are denser and less porous, which aids in rejecting salt more effectively. Adding nanoparticles to PSF helps to further enhance the hydrophilicity and rejection of contaminants, with lower ICP and fouling [16,25,29–34]. From the above observations reported in literature studies, it is evident that PBI and PSF are good choices for TFN membrane fabrication.

Integrated processes like FO/NF, NF/FO/RO and UF/FO/RO hybrid systems have been used for treating brackish water [35–37]. However, recovering water from the RO reject of brackish water by FO, which consumes less pumping power, is yet to be explored. Further, studies on treating RO reject of brackish water using PBI and PSF flat-sheet TFC and TFN membranes by FO are scarce. Therefore, the present study focuses on synthesising and applying PBI and PSF flat-sheet TFC and TFN membranes to recover water from RO reject using FO. The membranes were integrated with graphene-based non-functionalised MWCNT through non-solvent induced phase separation (NIPS). Using a laboratory-scale testing system, the performances of pristine PBI, pristine PSF, PBI/MWCNT and PSF/MWCNT membranes were compared. The impact of increasing MWCNT concentration on the membrane morphology, hydrophilicity, and mechanical, thermal, and intrinsic properties were analysed, in addition to FO performance. Optimal membrane composition and operating conditions were identified for the PBI and PSF flat-sheet membranes for water recovery from RO reject.

2. Materials and methods

2.1. Materials required for membrane fabrication

The materials required for the fabrication of the PBI and PSF TFN-based FO membranes in the laboratory are listed as follows: 100 g of PBI powder ($(C_{20}H_{12}N_4)_n$ with M_w : 308 g/mol, average M_w : $41,000 \pm 4000$ g/mol) was supplied by Sigma Aldrich, Bangalore, India, in pellet form; 100 g of PSF powder ($(C_{27}H_{21}O_4S)_n$ with M_w : 441 g/mol, average M_w : $22,000 \pm 3000$ g/mol) was supplied by Solvay India in pellet form; 100 g of polyvinylpyrrolidone (PVP) powder ($(C_6H_9NO)_n$ with M_w : 111 g/mol, average M_w : $360,000 \pm 3000$ g/mol); 50 g of lithium chloride powder (LiCl with M_w : 42.5 g/mol); 500 ml of n-dimethylacetamide (DMAc) solution (C_4H_9NO


Table 1
Composition of thin-film composite PBI membranes at different wt% of MWCNT.

Materials	Composition (wt%)			
	PBI	PBI/MWCNT ₁ wt%	PBI/MWCNT ₂ wt%	PBI/MWCNT ₃ wt%
PBI	18	17	16	15
LiCl	1.5	1.5	1.5	1.5
DMAc	80.5	80.5	80.5	80.5
MWCNT	0	1	2	3

Table 2
Composition of thin-film composite PSF membranes at different wt% of MWCNT.

Materials	Composition (wt%)			
	PSF	PSF/MWCNT ₁ wt%	PSF/MWCNT ₂ wt%	PSF/MWCNT ₃ wt%
PSF	18	17	16	15
PVP	2	2	2	2
DMF	80	80	80	80
MWCNT	0	1	2	3

Table 3
Analysis of the composition of RO reject water.

S. No.			Nemmeli Desalination Plant Brackish Water RO Brine Quality Details		
	Parameters	Method	Unit	FS	DS
1	Total Dissolved Solids	IS 3025 (Part 16) – 1984 (R 2017)	mg/l	37230	1428
2	Sodium as Na	IS 3025 (Part 45) – 1993 (R 2019)	mg/l	9830	782
3	Potassium as K	IS 3025 (Part 45) – 1993 (R 2017)	mg/l	412	89
4	Calcium as Ca	IS 3025 (Part 40) – 1991 (R 2019)	mg/l	496	134
5	Magnesium as Mg	IS 3025 (Part 46) – 1994 (R 2019)	mg/l	1374	157
6	Chloride as Cl	IS 3025 (Part 32) – 1988 (R 2019)	mg/l	16239	1670
7	Sulphate as SO ₄	IS 3025 (Part 24/Sec-1) – 2022	mg/l	2356	242
8	COD	IS 3025 (Part 58) – 2006 (R 2017)	mg/l	230	23
9	pH@25 °C	IS 3025 (Part 11) – 1983 (R 2002)	-log[H ⁺]	8.2	7.9

with M_w : 87 g/mol); 500 ml of *n*, *n*-dimethylformamide (DMF) solution (C_3H_7NO with M_w : 73 g/mol, 99.8 % purity); *m*-phenylenediamine (MPD, 99 % purity with M_w : 108.14 g/mol) and trimesoyl chloride (TMC, 98 % purity with M_w : 265.48 g/mol) were supplied from Sigma Aldrich; 75 g of multi-walled carbon nanotubes (MWCNT) was purchased from Ad Nano Technologies, Shimoga, Karnataka, India. For making the DS, 100 g of magnesium chloride (analytical grade $MgCl_2$ with M_w : 95 g/mol) purchased from SD Fine Chem Ltd, Mumbai, India, was used. RO reject of brackish water (10 L) collected from Nemmeli Seawater Desalination Plant, Tamil Nadu, India, was used as FS. Other substances used were: 500 g of sodium metabisulfite ($Na_2S_2O_5$ with M_w : 190 g/mol), deionised (DI) water (5 L), acetone AR grade (1 L C_3H_6O with M_w : 58 g/mol), toluene AR grade (1 L C_7H_8 with M_w : 92 g/mol), woven polyester and glass plate (1 ft × 1 ft).

2.2. Fabrication of PBI and PSF membranes

Following standard practice, the casting solution for the initial pristine PBI was prepared with 26 wt% PBI, 72.5 wt% DMAc and 1.5 wt% lithium chloride (LiCl). Similarly, the initial pristine PSF casting solution was prepared using 18 wt% PSF along with 2 wt% PVP being added as an agent for pore-forming and 80 wt% DMF [11,17,37–39]. However, at higher concentrations, particularly for PBI, membrane performance becomes inconsistent, as it is difficult to fabricate an asymmetric film of good quality due to increasing flow resistance and less solubility. Moreover, decreases in resistance to biological attacks, WF and membrane thickness are experienced at higher concentrations [39–41]. As a result, the concentrations of PBI were diluted to 14, 16, 18 and 20 wt% by adding more DMAc for performance comparison with 26 wt% PBI (Performance comparison results shown in Table 5 and Fig. 10a and b).

MWCNT was used with diameters of 20–80 nm and 3–8 μ m lengths. RO reject of brackish water was used as FS, while 2 M $MgCl_2$ was used as DS. PBI and PSF solutions were incorporated with different wt% of MWCNT (0–3 wt%). The polyamide active layers for the PBI and PSF membranes were prepared through an interfacial polymerisation (IP) reaction involving 0.2 wt% of TMC and 4 wt% of MPD. The reaction took 3 min to complete. MWCNT was then dispersed in 4 wt% MPD aqueous solution in an ultrasonic bath (Branson® ultrasonic bath (Danbury, Connecticut, United States)) for 4 h. Then, the MPD mixed with MWCNT was made to react with

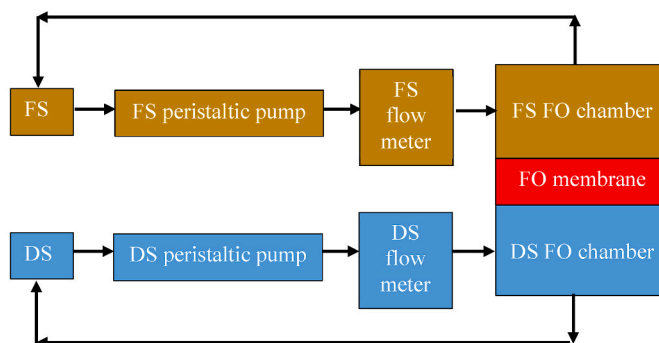


Fig. 1. (a) FO experimental laboratory-scale setup; (b) FO process schematic for the experimental setup.

0.2 wt% of TMC. Tables 1 and 2, respectively, present the composition of the PBI and PSF membranes at different wt% of MWCNT. Table 3 shows the typical composition of RO reject of brackish water (collected from Nemmeli Seawater Desalination Plant, Tamil Nadu, India) and the water purity analysis.

The membranes were fabricated as follows: 18 wt% of PBI was mixed with DMAc in the presence of LiCl to form the PBI casting solution. Similarly, 18 wt% of PSF was mixed with DMF in the presence of PVP to form the PSF casting solution. For fabricating the desired PBI/MWCNT and PSF/MWCNT casting solutions, MWCNT nanoparticles were added in the required percentage and dispersed with DMAc or DMF for 1 h through sonication using the ultrasonic bath at 50 °C. The concentrations of PBI were diluted to 17, 16 and 15 wt% using the MWCNT (1, 2 and 3 wt%, respectively) dispersed in DMAc. The concentrations of PSF were diluted to 17, 16 and 15 wt% using the MWCNT (1, 2 and 3 wt%, respectively) dispersed in DMF. The PBI, PSF, PBI/MWCNT and PSF/MWCNT casting solutions were then homogenised and continuously stirred at 60 °C and 150 rpm speed for 30 min. The solutions were degasified at room temperature for 24 h. The polymer solutions formed after degasification were poured on a fabric made of woven polyester, bound to a glass plate, and placed on a membrane casting machine with a heating apparatus. The film casting knife height was calibrated to 150 μm while the casting machine speed was set at 1 cm/s. The cast PBI and PBI/MWCNT films were kept in an oven for 1 min 30 s at 165 °C while PSF and PSF/MWCNT films were kept for 1 min 30 s at 70 °C. The cast membranes were laid inside a deionised (DI) water bath at room temperature for 15 min to begin phase inversion (PI). They were subsequently stored in 30 wt% of aqueous glycerol with sodium metabisulfite to prevent fouling and cracking [17,40].

2.3. Membrane characterisation

The PBI and PSF FO membranes were characterised based on their surface morphology, phase composition, water contact angle, presence of functional groups and chemical bonds, and mechanical stabilities.

For analysing the surface morphology and the elemental distribution of MWCNT in the PBI and PSF membranes, Scanning Electron Microscopy (SEM) was implemented to obtain images on the top surface (Model: JEOL JCM-6000 Plus). In SEM, micrographs were taken at 20 μm resolution with an accelerating voltage of 15 kV, WD10 mm, SEI 5X (WD56 mm to 53 mm) to 60,000X. All samples were sputter-coated with gold layers to observe them (SEM in Fig. 2a–h). Transmission Electron Microscopy (TEM) (Model: 200 kV Tecnai G² TF20) was employed to analyse the membrane morphology at a much closer range (TEM in Fig. 3a–f). The membranes were microtomed to 100 nm, and their electrons were made transparent on copper grids. Energy dispersive X-ray spectroscopy (EDS) was implemented to detect the composition of elements in the membranes (Model: INCA x-act analytical 10 mm² silicon drift detector with PentaFET precision) (EDS in Fig. 4a–h).

To study the MWCNT phase composition, an X-ray diffraction (XRD) analyser (Model: Japan-based XRD-2kW-RIKAGU Miniflex 600) was implemented. CuK α radiation was applied with 2θ ranging from 10° to 80°, using a step size of 0.05° (XRD in Fig. 5). Fourier transform infrared spectroscopy (FTIR) was used to determine the functional groups present and chemical bonds formed in the

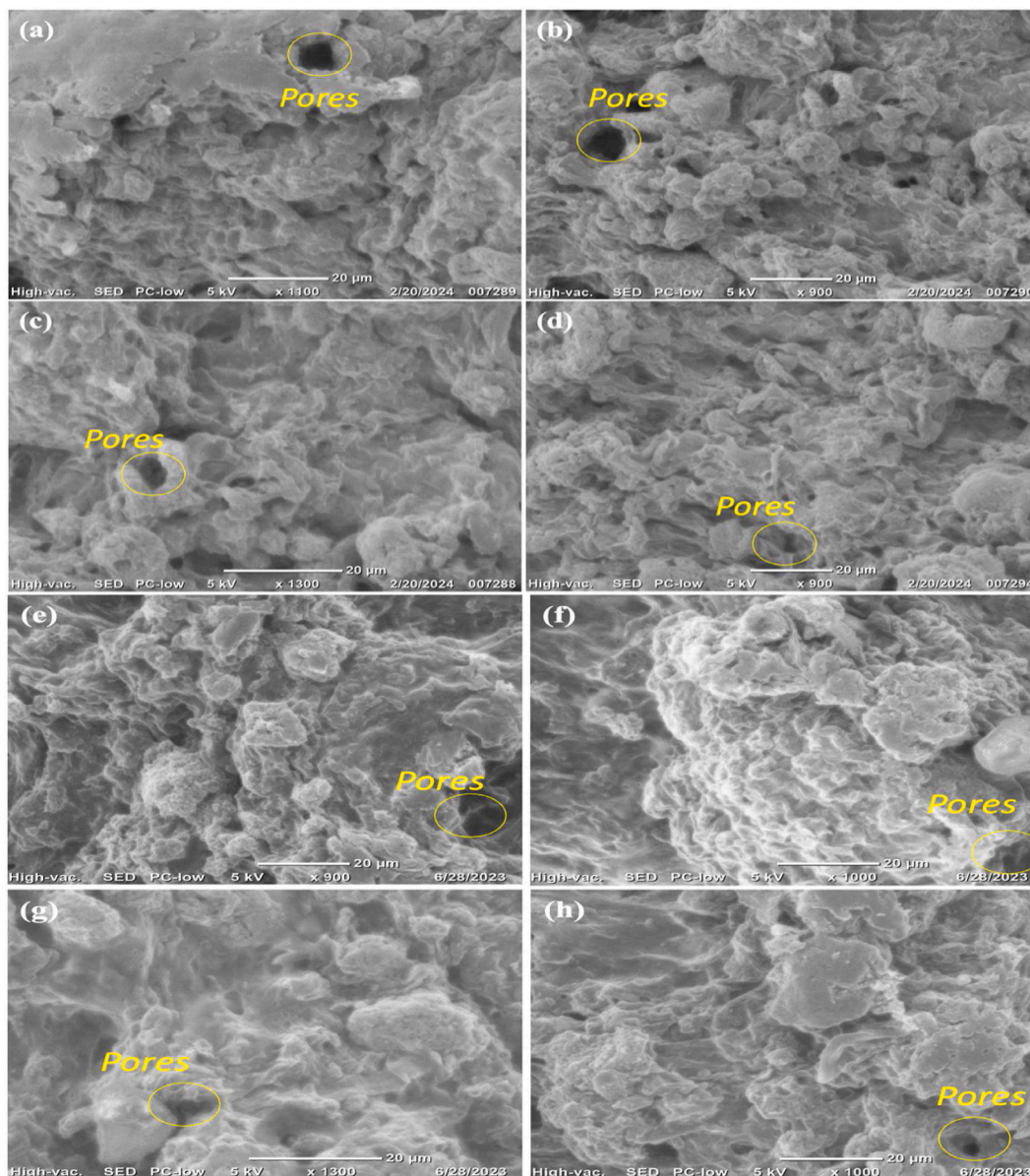


Fig. 2. SEM images for (a) PBI; (b) PBI/MWCNT₁ wt%; (c) PBI/MWCNT₂ wt%; (d) PBI/MWCNT₃ wt%; (e) PSF; (f) PSF/MWCNT₁ wt%; (g) PSF/MWCNT₂ wt%; (h) PSF/MWCNT₃ wt% FO membranes.

membrane. The results were observed and recorded using an FTIR spectrometer (Model: IRAffinity-1S from Shimadzu, Japan), where the frequency range was measured as wave numbers typically between 4000 and 500 cm^{-1} (FTIR in Fig. 6a and b).

For studying the membrane surface water contact angles to determine the level of their hydrophilicity, a contact angle measuring drop shape analyser (Model: DSA 25 from Krüss, Germany) was employed. The contact angle measurements were performed on five random locations along the surface of each membrane sample as reference points (Contact angle measurements in Fig. 7a and b). For analysing the thermal stability of the membrane, a thermal analyser (Model: SDT650 simultaneous DSC-TGA analyser) was implemented (DSC in Fig. 8a and b, TGA in Fig. 9a and b). The mechanical properties, such as the elongation, tensile strength, and modulus of elasticity/Young's modulus, were determined using a load cell of 10 kN at a strain rate of 1 mm/min. The dual-column testing system tested the elongation and strength (Model: Instron 5966, Massachusetts, USA). The samples were cut up in the shape of dog bones (16 cm in length and 3.3 cm in width) using a hand-operated Ray-Ran press. The specimens were 30–100 μm thick, and a micrometre was used to measure the dimensions (Mechanical properties values in Table 4).

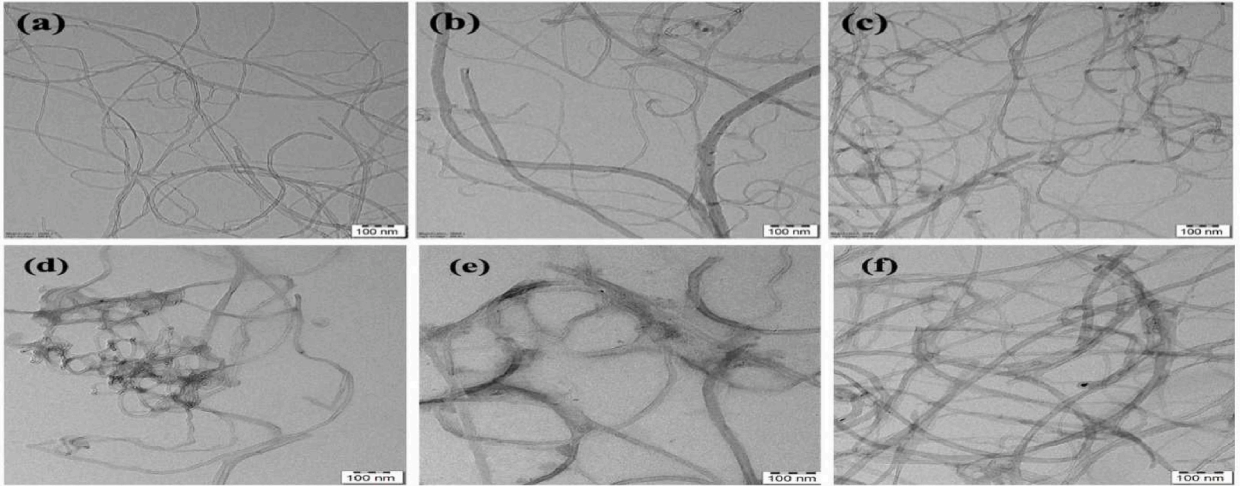


Fig. 3. TEM analysis for (a) PBI/MWCNT₁ wt%; (b) PBIMWCNT₂ wt%; and (c) PBI/MWCNT₃ wt%; (d) PSFMWCNT₁ wt%; (e) PSF/MWCNT₂ wt%; (f) PSF/MWCNT₃ wt% FO membranes.

2.4. Experimental setup of the process

The laboratory-scale setup for the FO experiment and its schematic are shown in Fig. 1a and b, respectively. The setup comprised two rectangular flow channels, each having 15 cm length, 10 cm breadth and 0.4 cm height. The cross-sectional area for each membrane was 150 cm². The membranes were pre-compacted using an applied pressure of 3 bar to stabilise the WF. Mesh spacers made of woven polyester were placed in the rectangular channels to elevate the turbulence level, promote mass transport, and assist the membrane in reducing the external concentration polarisation (ECP) [16,17,29]. The FS and DS were introduced into the FO chamber with equal flow rates of 48 mL/min by co-currently using two peristaltic pump motors (Model: VENUS AQUA® U6600 Power Head Water Aquarium Motor). Using 2 M MgCl₂ as DS, the PBI, PSF, PBI/MWCNT and PSF/MWCNT membranes were tested. The crossflow velocity was 0.67 cm/s. The results were documented with two different orientation types for the membranes: The active layer was oriented (1) towards the FS and (2) towards the DS. With the membrane inside, the FO chamber was set up horizontally with the FS and DS in the top and bottom compartments, respectively. The FS and DS concentrations were constant during the experiment by closed-loop circulation. The experiment was conducted at room temperature with 30-min time intervals for each sample.

2.5. Equations used for FO water transport analysis

The idealised van't Hoff equation, which helps to derive the FS and DS osmotic pressures, is given by:

$$\pi = iCRT \quad (1)$$

Where i denotes the van't Hoff factor, R represents the universal gas constant (0.08314 L bar/K.mol), T refers to the process temperature (K), and C indicates the solute molar concentration (mol/L). The molar concentration term C has a direct, linear connection with π since i , R , and T remain constant for the most part. For the concentrations of the solutions taken into consideration here, this was a realistic assumption [42].

Water flux WF is denoted by the units L/m².h or LMH. The water mass flow rate obtained from the experiment is divided by density to evaluate the volumetric flow rate. Flux is evaluated by scaling this flow rate by the membrane area [42]. The theoretical equation for WF (or J_w) is derived from Darcy's law of fluid flowing through a porous medium and is given by:

$$J_w = A(\Delta\pi - \Delta P) = A((\pi_d - \pi_f) - \Delta P) \quad (2)$$

Here A (LMH/bar) indicates the membrane permeability coefficient for water, $\Delta\pi$ (bar) denotes the difference between osmotic pressures, ΔP (bar) represents the applied external pressure difference, π_d and π_f both respectively denote the osmotic pressures for the DS and FS [40,42–44]. The WF is calculated by measurement of the weight changes in the FS via a digital weighing machine [16,17,40]. WF can also be expressed as shown below:

$$J_w = \frac{(V_0 - V_e)}{A_m \Delta t} \quad (3)$$

Where V_0 and V_e are the feed side volumes before and after completing the experiment, A_m denotes the effective membrane area and Δt indicates the time interval (min) [16,17,40].

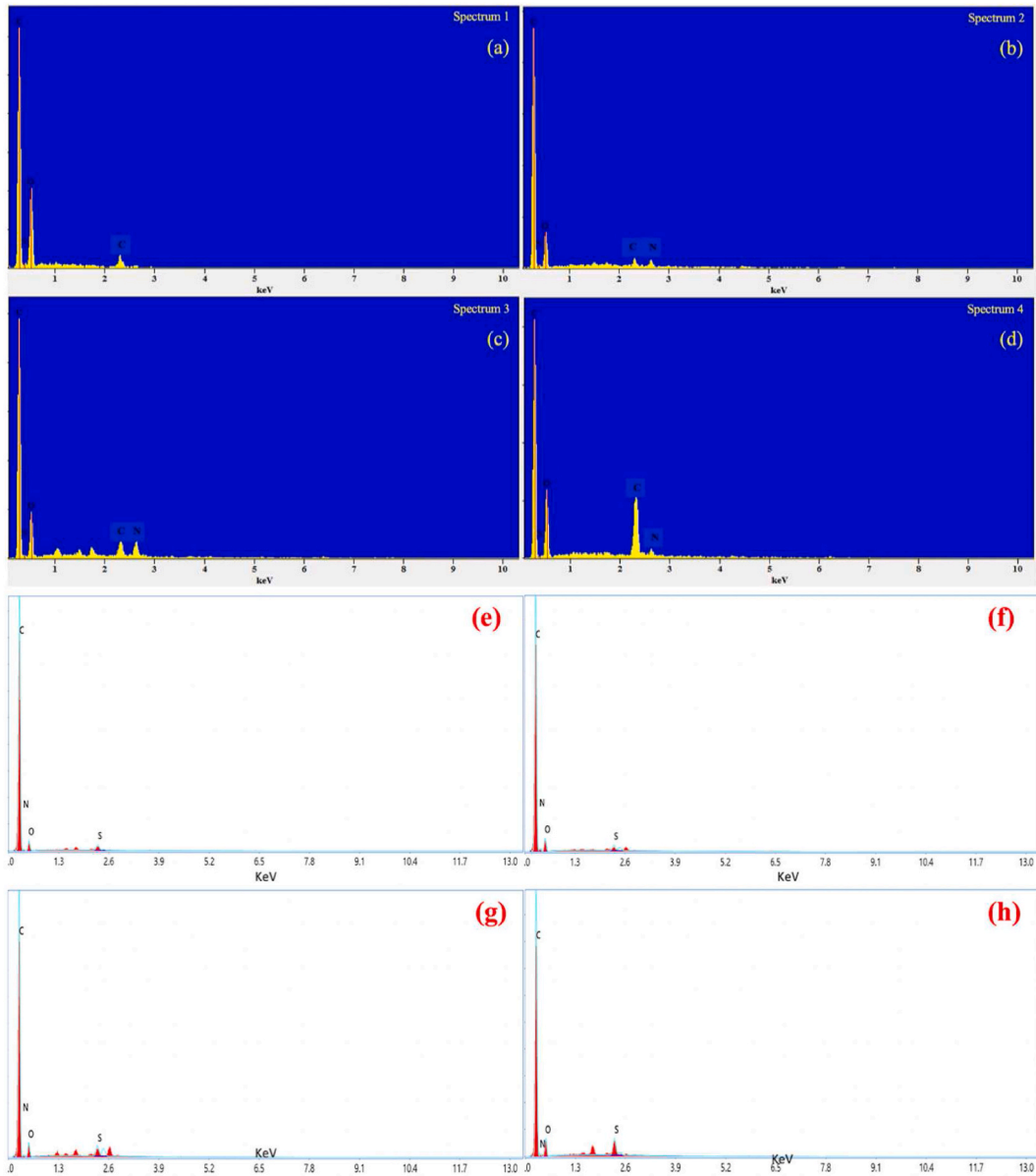


Fig. 4. EDS analysis images for (a) PBI; (b) PBI/MWCNT₁ wt%; (c) PBI/MWCNT₂ wt%; (d) PBI/MWCNT₃ wt%; (e) PSF; (f) PSF/MWCNT₁ wt%; (g) PSF/MWCNT₂ wt%; (h) PSF/MWCNT₃ wt% FO membranes.

The RSF (or J_s), refers to the reverse transfer of solute which impedes the water passage across the membrane and increases the FS osmotic pressure, thus lowering the overall $\Delta\pi$ value. The RSF is calculated as shown below:

$$J_s = \frac{(V_e C_{f,e} - V_e C_{f,0})}{A_m \Delta t} \quad (4)$$

Where $C_{f,e}$ and $C_{f,0}$ are the FS concentrations at the end and beginning of the experiment, and V_e denotes the FS volume at the end [40]. The conductivity of both FS and DS were measured via an HQ40d multimeter (Hach Lange GmbH, Germany) to determine the RSF values [15,16,28].

The salt permeability (B) (10^{-12} m/s.pa) and the salt rejection rate (R_s) (%) were measured using equations (5) and (6). Here, C_p represents the concentration of permeate product water.

$$B = \left[\frac{1 - R_s}{R_s} \right] \times J_w \quad (5)$$

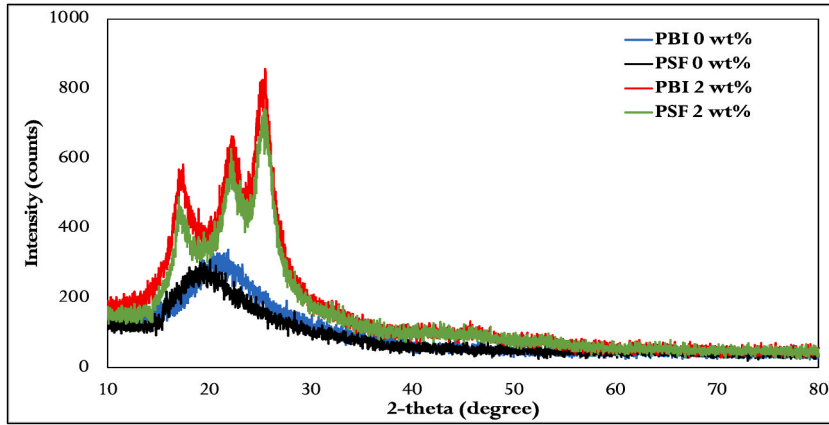


Fig. 5. XRD plots for PBI, PSF, PBI/MWCNT₂ wt% and PSF/MWCNT₂ wt% membranes.

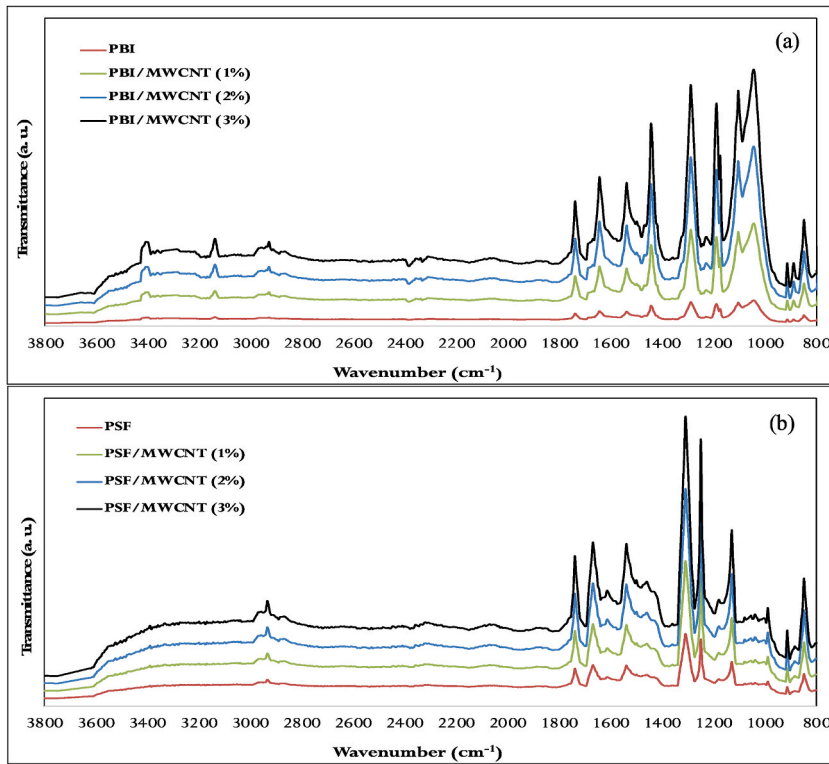


Fig. 6. FTIR plots for (a) PBI membranes; (b) PSF membranes.

$$R_s = \left[\frac{C_f - C_p}{C_f} \right] \times 100 \quad (6)$$

The formula for structural parameter (S) (mm) estimates the path length for diffusion of water through the FO membrane, which determines the degree of ICP during the FO process, is given by:

$$S = \frac{\tau l}{\varepsilon} \quad (7)$$

Where ε (%) denotes the overall porosity, τ represents the tortuosity ($1 < \tau < 2$), and l (mm) is the membrane thickness [29,40].

The FO membrane porosity, which refers to the FO membrane pore volume divided by the entire membrane volume, is calculated through gravimetric measurement as shown below:

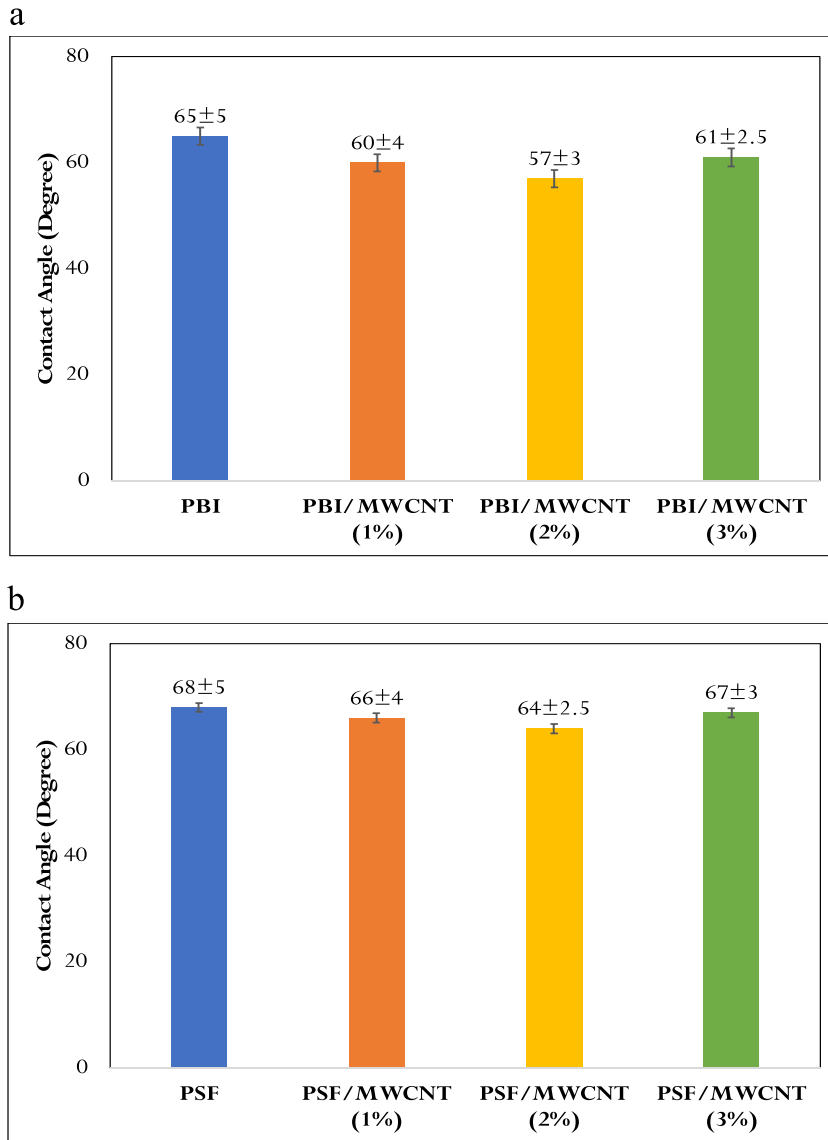


Fig. 7. a. Water contact angle measurements for PBI membranes
b. Water contact angle measurements for PSF membranes.

$$\varepsilon = \frac{(m_{wet} - m_{dry})/\rho_w}{((m_{wet} - m_{dry})/\rho_w) + ((m_{dry})/\rho_p)} \times 100 \% \quad (8)$$

Where m_{dry} and m_{wet} , respectively, represent the dry mass and wet mass of membranes, and ρ_p and ρ_w denote polymer and water densities, respectively [17,40].

3. Results and discussions

3.1. Surface morphologies of the FO membranes

The SEM images in Fig. 2a–h displays the top surface morphological characteristics of the fabricated PBI and PSF FO membranes. The images depict the ridge valley-type structure formed on top of PBI and PSF, typical for TFC and TFN membranes, because of the IP reaction between TMC and MPD [29,40]. The pore size is observed to decrease with an increase in wt% of MWCNT. This could be attributed to the MWCNT exhibiting strong attractive molecular forces due to their nano size. These forces result in pore size reduction and material compaction. The decrease in pore size can potentially cause a decrease in both WF and salt rejection rates; however, the tendency for WF reduction is more than compensated by the greater affinity to water shown by PBI due to the strong hydrogen bonding

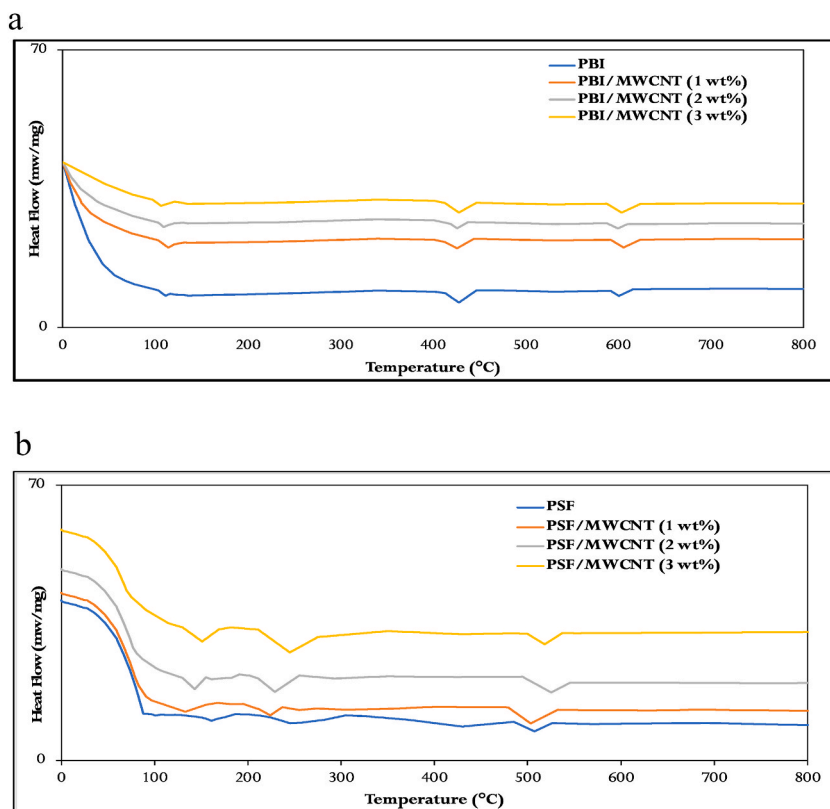


Fig. 8. a. DSC graph for PBI membranes
b. DSC graph for PSF membranes.

of PBI molecules [45,46]. The polyamide active layer is observed to appear as the wt% of MWCNT increases, which results in increased salt rejection until 2 wt%. Although thin active layers are good for improving the WF, they sometimes tend to decrease salt rejection in a significant manner. An ideal FO membrane must possess an active layer that is thin, hydrophilic, dense, with high WF and an efficient salt rejection rate [29]. In contrast, its support layer should have low tortuosity and be porous to mitigate ICP. Therefore, strengthening the FO membrane surface hydrophilicity is preferable to decreasing its thickness; this is because higher hydrophilicity improves WF without increasing the RSF [17]. The difference in the morphology of the PSF FO membranes by adding MWCNT is attributed to hydrogen bonds formed between the polyamide chains and MWCNT. This, in turn, improves the hydrophilicity of PSF [40]. However, the intermolecular π - π interactions between PBI and MWCNT result in PBI showing slightly better hydrophilicity than PSF. This is reflected in the transmission electron microscopy (TEM) images and the contact angle measurements [47–49].

3.2. TEM analysis

The TEM analysis for PBI and PSF membranes was conducted as shown in Fig. 3a–f. The TEM images show the distribution of the MWCNT in PBI and PSF membranes more explicitly. These depictions for both PBI and PSF FO membranes convey that MWCNT is uniformly distributed in the FO membranes without much agglomeration until 2 wt%. The diameters of the MWCNT remain constant, and no confined areas are detected in the vicinity of MWCNT due to the MWCNT being hydrophilic up to 2 wt%. The lengths of the MWCNT are observed to be relatively short, favouring the increase in WF. In both PBI and PSF membranes, MWCNT nanoparticles are not open-capped, indicating that they are non-functionalised. The MWCNT in PSF tend to agglomerate more than in PBI, and the distribution of the nanoparticles is more uniform in PBI than in PSF. Adding MWCNT also influences the membrane wettability, with the contact angle decreasing with increasing wt% of MWCNT until 2 wt%. This increases the hydrophilicity of the membranes for water transport, subsequently leading to an increase in WF and a reduction of RSF values [40,50–52].

3.3. Elemental distribution of the FO membranes

To ascertain the distribution of elements and composition of MWCNT in the PBI and PSF FO membranes, energy dispersive X-ray spectroscopy (EDS) was implemented, as seen in Fig. 4a–h. The EDS images of PBI membranes display the peaks for oxygen (O), nitrogen (N) and carbon (C), which appear as expected since the PBI molecule consists of the imidazole ring containing nitrogen. As for the PSF membranes, the additional presence of sulphur (S) is expected because of the sulphonyl group in PSF. The high carbon content

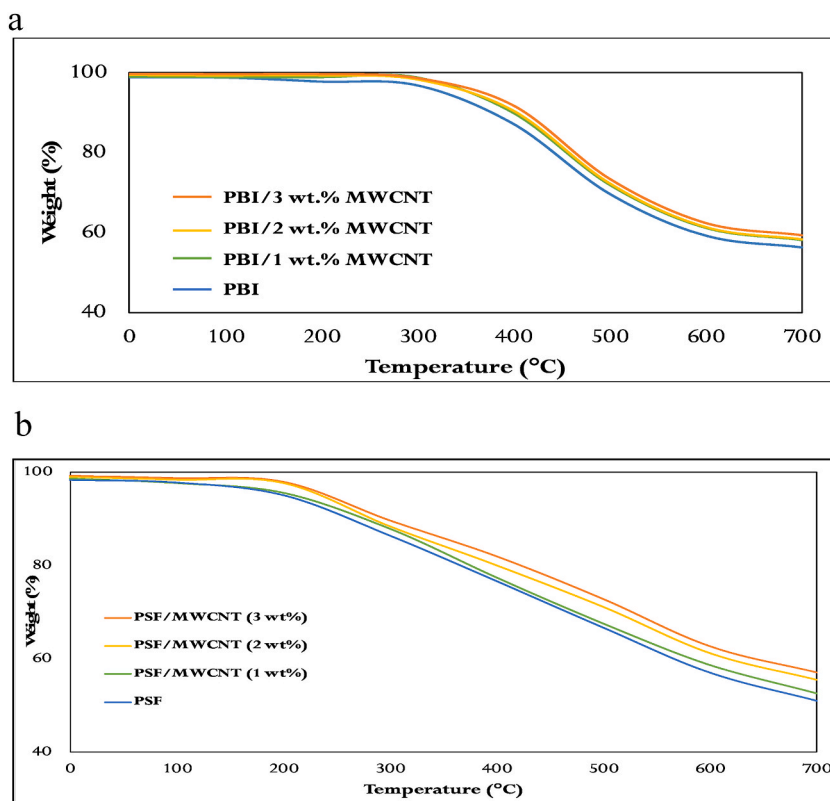


Fig. 9. a. TGA graph for PBI membranes
b. TGA graph for PSF membranes.

in both PBI and PSF membranes is also likely due to the addition of MWCNT. The high carbon-to-oxygen ratio implies negligible alginate fouling on the membrane surface. Although carbon-to-oxygen (C:O) atomic ratio decreases, the C:O ratio values are high enough to conclude that fouling is negligible [15]. The negligible amount of fouling can make the membranes more resistant to biological attacks and subsequently enhance their performance, particularly with respect to porosity and WF [15].

3.4. XRD analysis

The X-ray diffraction (XRD) image for the PBI and PSF membranes is depicted in Fig. 5, with diffraction peaks in between 2θ range of $14\text{--}25^\circ$ for PBI and $12\text{--}20^\circ$ for PSF. The two sharp peaks at $2\theta = 26^\circ$ confirm the presence of MWCNT and illustrate the stronger orientation of the reinforcement with the improved crystalline nature of the PBI/MWCNT_{2 wt%} and PSF/MWCNT_{2 wt%} membranes. The improvement in crystallinity of PBI and PSF membranes after adding MWCNT increases the mechanical and thermal stabilities. Additionally, it reduces RSF and causes an increase in porosity and WF [53,54].

3.5. FTIR spectra of the membranes

The analysis of the FTIR graphs in Fig. 6a depicts characteristic peaks representing the amine (C–N stretch) at 1540 cm^{-1} and aromatic bond (C=C & C=N) at 1645 cm^{-1} . The peaks seen at 3400 cm^{-1} and 3140 cm^{-1} represent the free (N–H) and H-bonded (N–H) stretches, respectively. The prominent peaks visible at 1445 cm^{-1} and 1290 cm^{-1} , respectively, display the imidazole ring in-plane deformation and the imidazole ring breathing mode. The rising peaks at 1310 cm^{-1} , 1290 cm^{-1} and 1135 cm^{-1} for PSF membranes in Fig. 6b show that sulfone stretches (S=O) are present. The small peaks at 3000 cm^{-1} indicate aromatic (C–H) bond stretches for the PBI and PSF membranes. The carboxyl (C=O) bond indicates MWCNT in PBI appears at 1735 cm^{-1} and 1670 cm^{-1} in PSF. The C=O peak increases with increase in wt% of MWCNT. The FTIR analysis of PBI and PSF synthesised in this investigation is consistent with the ones in the literature, in addition to confirming the physical presence of MWCNT in the membranes as in XRD, which also implies an increase in their crystallinity [47,48,55].

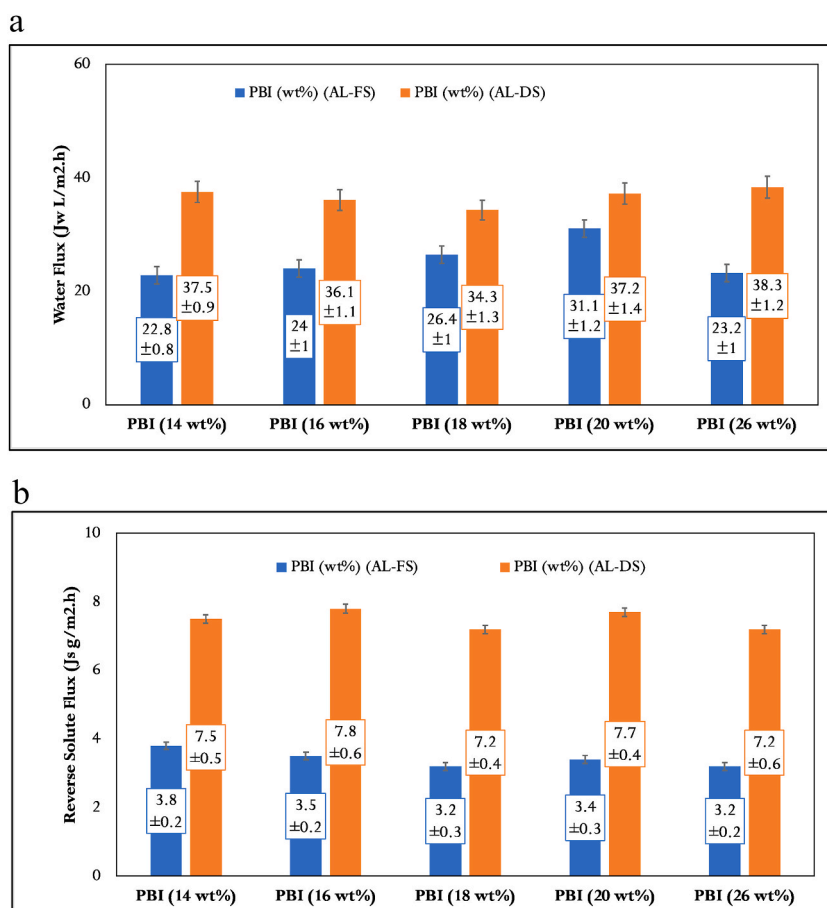


Fig. 10. a. Graph of WF comparing PBI membranes at different concentrations
b. Graph of RSF comparing PBI membranes at different concentrations.

Table 4

Mechanical behaviour of PBI and PSF FO membranes.

Membrane	Elongation (%)	Modulus of elasticity (MPa)	Tensile strength (MPa)
PBI	27.8 ± 3.4	426 ± 34	29.3 ± 5.5
PBI/MWCNT (1%)	24.6 ± 2.2	472 ± 53	32.5 ± 4.6
PBI/MWCNT (2%)	20.1 ± 3.1	565 ± 40	37 ± 2.4
PBI/MWCNT (3%)	18.6 ± 1.9	610 ± 45	38.6 ± 3
PSF	25.9 ± 2.9	411 ± 31	26.6 ± 4.1
PSF/MWCNT (1%)	21.7 ± 2.1	440 ± 47	29.4 ± 4
PSF/MWCNT (2%)	18.3 ± 2.8	512 ± 31	33.3 ± 2.2
PSF/MWCNT (3%)	16.7 ± 2.3	577 ± 38	35.5 ± 2.9

3.6. Measurement of water contact angle

The water contact angles for both PBI and PSF membranes are represented graphically in Fig. 7a and b. The contact angle decreases when MWCNT is added, resulting in higher hydrophilicity of the PBI and PSF membranes. The contact angle of PBI and PSF increased when 3 wt% of MWCNT was added to their respective casting solutions. This is due to the agglomeration of MWCNT on the membrane surface, which is also confirmed in previous literature studies [48,49]. PBI shows slightly higher hydrophilicity than PSF due to the strong hydrogen bonds between adjacent PBI molecules and the strong intermolecular π - π interactions between PBI and MWCNT. This is also reflected in the corresponding SEM and TEM images and the increase in WF and porosity values of the membranes [45–49].

Table 5
SRSF values of PBI FO membranes.

Membrane	SRSF (J_s/J_w) (AL-FS)	SRSF (J_s/J_w) (AL-DS)
PBI (14 wt%)	0.1667	0.2
PBI (16 wt%)	0.1458	0.2161
PBI (18 wt%)	0.1212	0.2099
PBI (20 wt%)	0.1093	0.207
PBI (26 wt%)	0.1379	0.1879

Table 6
Porosities for PBI and PSF FO membranes.

Membrane	Surface morphology	Porosity (ϵ) (%)	S Value (mm)	Salt rejection rates (R_s) (%)
PBI	Ridge Valley	64 \pm 2	0.41 \pm 0.1	81.3
PBI/MWCNT (1%)	Ridge Valley	66 \pm 2	0.38 \pm 0.05	89.8
PBI/MWCNT (2%)	Ridge Valley	70 \pm 4	0.36 \pm 0.2	93.5
PBI/MWCNT (3%)	Ridge Valley	67 \pm 3	0.39 \pm 0.1	90.3
PSF	Ridge Valley	61 \pm 2	0.43 \pm 0.1	77
PSF/MWCNT (1%)	Ridge Valley	63 \pm 3	0.41 \pm 0.1	87.1
PSF/MWCNT (2%)	Ridge Valley	66 \pm 2	0.40 \pm 0.05	89.6

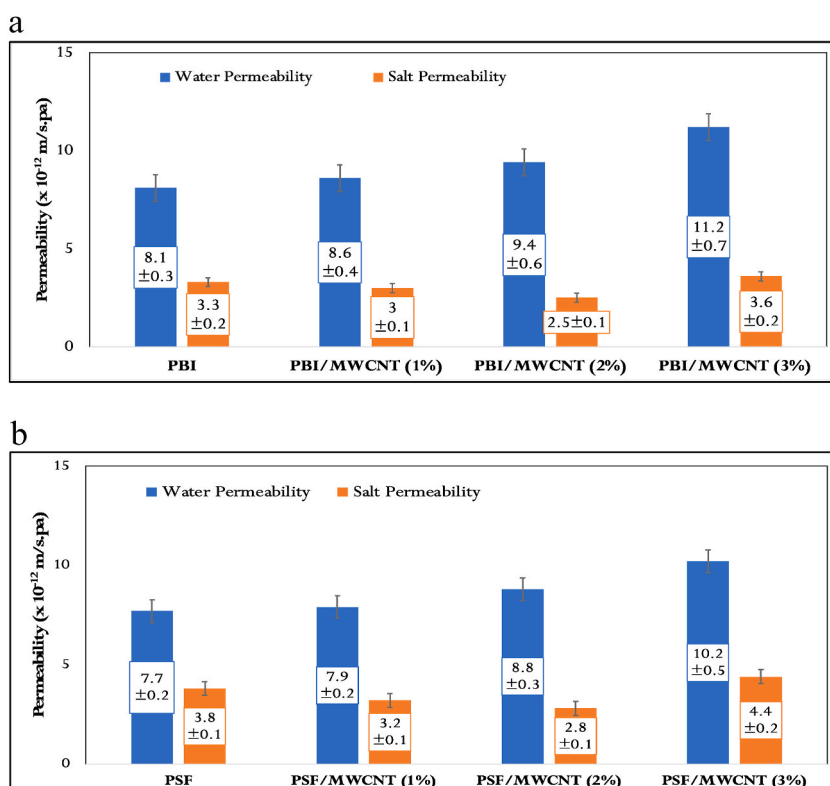


Fig. 11. a. Permeability graph of PBI membranes
b. Permeability graph of PSF membranes.

3.7. Thermal stability of the FO membranes

The differential scanning calorimetry (DSC) diagrams for both PBI and PSF FO membranes are shown in Fig. 8a and b. In comparison, the thermogravimetric analysis (TGA) diagrams for both PBI and PSF are shown in Fig. 9a and b. For the DSC of PBI, the glass transition temperature (T_g) is at 420–425 °C while the melting temperature (T_m) is above 600 °C [56,57]. For the DSC of PSF, the T_g lies between 190 and 230 °C while T_m is in the range of 500–520 °C [58–60]. The interfacial interaction of the MWCNT comes into play for both PBI and PSF. In the TGA, the initial decomposition temperature of PSF is in the range of 190 °C–250 °C and the temperatures for varying weight losses of 10 and 20% correspond to the ranges of 210 °C–225 °C and 295 °C–310 °C respectively. It is observed that PBI

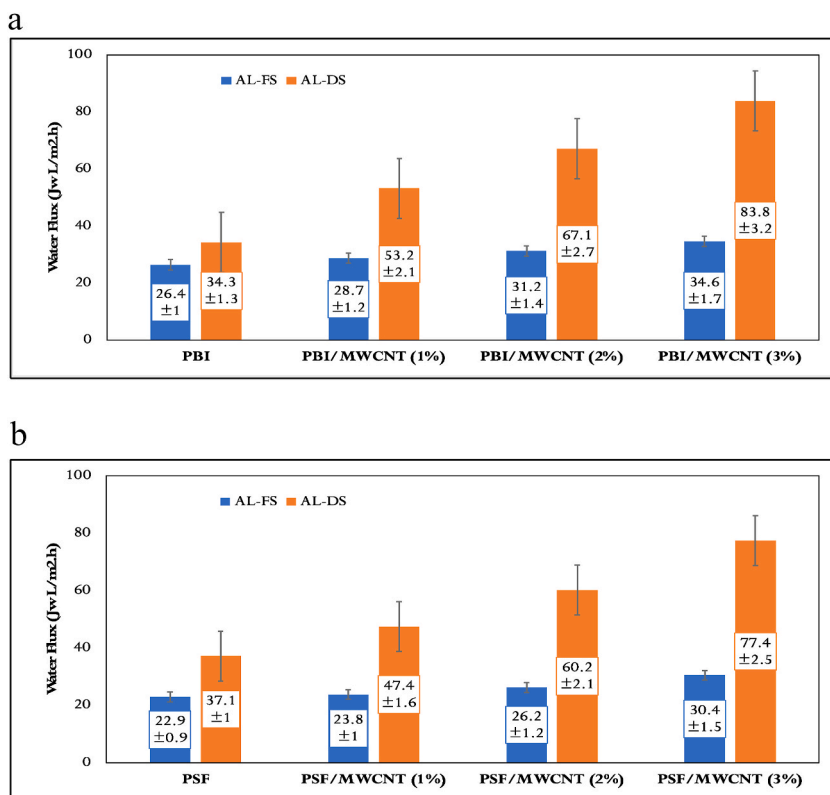


Fig. 12. a. Graph of water flux for PBI membranes
b. Graph of water flux for PSF membranes.

and PSF membranes are thermally stable. In the TGA, the initial decomposition temperature of PBI is in the range of 360 °C–440 °C, and the temperatures for varying weight losses of 10 and 20% exist in the ranges of 377 °C–382 °C and 421 °C–425 °C respectively. Since MWCNT possess higher thermal conductivity because of their strong intermolecular forces, heat flow is enhanced by adding MWCNT, as it takes more time to arrive at a steady state. PBI membranes exhibit better thermal stability owing to the suitable interfacial interactions of the MWCNT, with the hydrogen bonding between PBI molecules and intermolecular π – π interactions between PBI and MWCNT reducing the water contact angles (until 2 wt%), improving the hydrophilicity and overall performance [56–60].

3.8. Mechanical behaviour

The properties that describe the mechanical behaviour of the PBI and PSF membranes are shown in Table 4. The mechanical properties increase with the addition of MWCNT, which further indicates that the PBI and PSF FO membranes are mechanically stable. PBI shows slightly more enhanced mechanical strength characteristics than PSF. This can be attributed to the hydrogen bonds in the PBI molecules in addition to the higher intermolecular forces of MWCNT with PBI, which render the PBI/MWCNT membranes more tightly packed. The reduction in pore size causes material compaction, which enhances the mechanical properties of the membrane. The crystallinity also improves, which is reflected in the peaks shown in the XRD for PBI and PSF upon adding MWCNT [17,39,40].

3.9. Determination of the performances of FO membranes

The results for WF and RSF are seen in Fig. 10a and b, respectively, while the values of the specific reverse solute flux (SRSF) are shown in Table 5. For AL–FS orientation, the WF enhances with increase in PBI concentration until 20 wt% and then decreases at 26 wt%; for AL–DS orientation, the WF decreases with an increase in PBI concentration until 18 wt% and then increases from 20 wt% onwards. This is because pristine PBI membranes with high wt% of PBI are challenging to fabricate into asymmetric flat-sheet membranes of excellent and consistent quality. Due to this, minor inconsistent variations in WF are observed at high polymer concentrations. However, these variations are not significant. With respect to RSF, the values of PBI at 18 wt% and 26 wt% are the lowest and also identical. The SRSF values show that 20 wt% and 26 wt% PBI are the lowest for AL–FS and AL–DS orientations. However, the SRSF for 18 wt% PBI in the AL–FS orientation is lower than that of 26 wt% PBI. The lower the SRSF, the better the membrane performance [17]. In general, considering the values of WF, RSF and SRSF, 18 wt% PBI is found to have better performance, and hence, it is implemented as the pristine PBI membrane in this investigation.

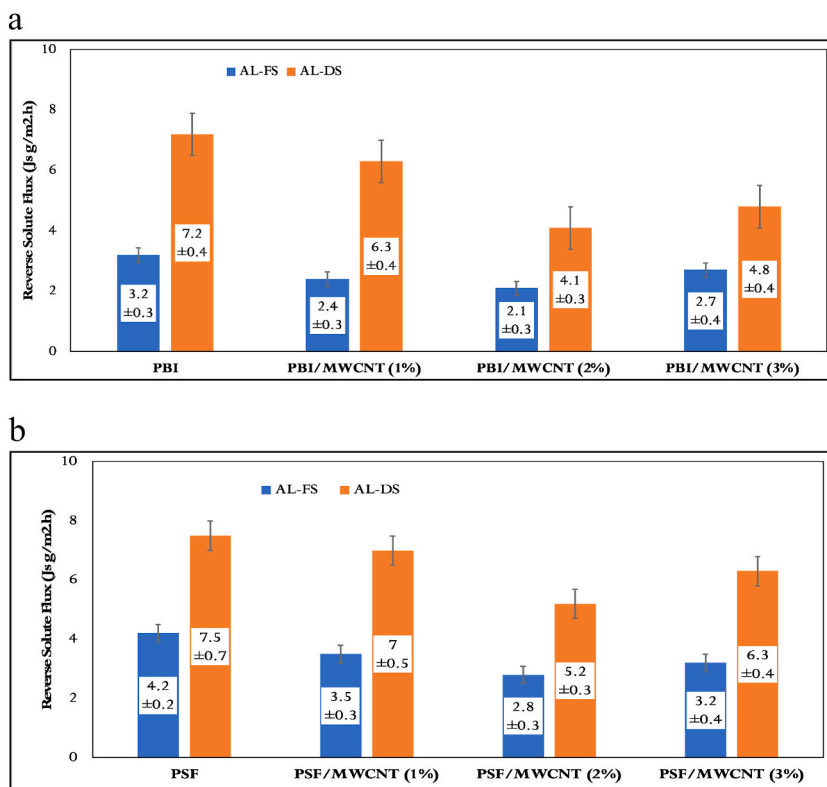


Fig. 13. a. Graph of reverse solute flux for PBI membranes
b. Graph of reverse solute flux for PSF membranes.

The porosity (ϵ), structural parameter (S) and salt rejection rate (R_s) values of the PBI and PSF membranes are seen in Table 6. The porosity for the PBI and PSF membranes increases with the addition of MWCNT despite the reduction in pore size. The increase in porosity is effective with the MWCNT addition till 2 wt%, beyond which MWCNT agglomeration sets in. The beneficial effects with respect to the enhancement of WF and salt rejection can be attributed to the membrane morphological characteristics changing with the addition of MWCNT. The S values decrease, signifying lower tortuosity. This, in addition to increase in porosity, decrease in pore size and higher hydrophilicity, improves the overall performance of the PBI/MWCNT and PSF/MWCNT membranes in comparison to the corresponding pristine membranes. The MWCNT seem to agglomerate after 3 wt%, adversely affecting the membrane performance through an increase in S value and decrease in porosity and salt rejection rate [17,29,39,49]. Fig. 11a and b shows the values of water and salt permeabilities for PBI and PSF membranes, respectively. The water permeability is seen to increase upon adding MWCNT from 1 to 3 wt%. For salt permeability, an increase is seen with MWCNT addition till 2 wt%, and a decrease in value occurs at 3 wt% due to pore size reduction [17,26,50]. The WF graphs shown in Fig. 12a and b illustrate that it increases with the addition of MWCNT wt%, with higher values for PBI membranes than for PSF membranes. In the presence of MWCNT, the PBI membrane becomes more hydrophilic. Fig. 13a and b depict the RSF values of PBI and PSF. As more water flows through the membrane with the addition of MWCNT, a synergetic effect of reduction in RSF occurs. However, other contaminants were not allowed to pass through. The values of RSF for both PBI and PSF decrease until 2 wt% and then increase at 3 wt%. This is attributed to the agglomeration of MWCNT in the membranes, which is also reflected in the water contact angle increasing at 3 wt%. Compared to pristine PBI and PSF, PBI/MWCNT and PSF/MWCNT have higher hydrophilicity and permeability and exhibit lower water contact angles until 2 wt%, as seen in Fig. 7a and b. The RSF values of PBI membranes are slightly lower when compared to those of PSF. All these factors show that the PBI membranes display marginally better WF and salt rejection rates than the PSF membranes [16,39]. Among the different membrane samples investigated, the membrane with the best overall performance is observed to be PBI/MWCNT_{2 wt%}. The porosity of this membrane is $70 \pm 4\%$, while its S and R_s values are $0.36 \pm 0.2 \mu\text{m}$ and 93.5% , respectively. Also, the WF values of 31.2 ± 1.4 LMH (for AL-FS) and 67.1 ± 2.7 LMH (for AL-DS) are observed to be 15% and 49% higher than the pristine PBI membrane, respectively. The corresponding RSF values of $2.1 \pm 0.3 \text{ g/m}^2\text{.h}$ (for AL-FS) and $4.1 \pm 0.3 \text{ g/m}^2\text{.h}$ (for AL-DS) are observed to be 34% and 43% lower than those of the pristine PBI membrane, respectively.

3.10. Comparison of PBI and PSF FO membrane performances

The performances of PBI/MWCNT_{2 wt%} and PSF/MWCNT_{2 wt%} FO membranes observed in our investigation were compared with performances reported in other literature studies and are presented in Tables 7a and 7b, respectively.

Table 7

a. Comparison of performance of PBI FO membrane reported in this investigation and those in published literature
 b. Comparison of performance of PSF FO membrane reported in this investigation and those in published literature.

Type of membrane	Incorporated nanoparticle	FS	DS	J_w (LMH)	J_s (g/m ² .h)	Ref
PBI flat sheet TFN	MWCNT (2 wt%)	RO reject of brackish water	2 M MgCl ₂	31.2 ± 1.4 (for AL-FS) 67.1 ± 2.7 (for AL-DS)	2.1 ± 0.3 (for AL-FS) 4.1 ± 0.3 (for AL-DS)	this work
PBI flat sheet TFC	–	DI	2 M MgCl ₂	21.28 ± 0.2 (for AL-DS)	7.82 (for AL-DS)	[17]
PBI flat sheet TFC	–	0.1 M NaCl	2 M NH ₄ HCO ₃	~2 (for AL-FS) ~18 (for AL-DS)	–	[34]
PBI flat sheet TFN	SiO ₂ (0.5 wt%)	DI	2 M NaCl	16.9 ± 1.2 (for AL-DS)	~45 (for AL-DS)	[49]
Type of membrane	Incorporated nanoparticle	FS	DS	J_w (LMH)	J_s (g/m ² .h)	Ref
PSF flat sheet TFN	MWCNT (2 wt%)	RO reject of brackish water	2 M MgCl ₂	26.2 ± 1.2 (for AL-FS) 60.2 ± 2.1 (for AL-DS)	2.8 ± 0.3 (for AL-FS) 5.2 ± 0.3 (for AL-DS)	this work
PSF TFN	f-MWCNT (0.5 wt%)	DI	2 M MgCl ₂	15.3	9.5	[16]
PSF flat sheet TFN	f-MWCNT (0.05 wt%)	DI	2 M NaCl	30 (for AL-FS)	2.86 ± 0.4 (for AL-FS)	[29]
PSF flat sheet TFN	carboxylated f-MWCNT (0.01 wt%)	DI	2 M NaCl	50.23 ± 0.93 (for AL-FS)	2.76 ± 0.21 (for AL-FS)	[40]
PSF flat sheet TFN	TiO ₂ (0.5 wt%)	10 mM NaCl	2 M NaCl	29.7 (for AL-FS) 56.27 (for AL-DS)	7.3 (for AL-FS) 14.14 (for AL-DS)	[60]

4. Conclusions

The present experimental investigation was conducted with PBI and PSF TFN-based FO membranes with the addition of MWCNT to recover water from the RO reject of brackish water. The membranes were characterised by their morphology, hydrophilicity, mechanical, thermal, and intrinsic properties, and water separation performance. The morphology analysis reveals that MWCNT is uniformly distributed. Pore size reduction is observed due to its attractive intermolecular forces. The affinity for PBI and PSF membranes towards water is due to their tendency to form hydrogen bonds with both water and MWCNT, as well as the intermolecular π - π interactions between PBI and MWCNT. Consequently, the contact angle of the PBI/MWCNT and PSF/MWCNT membranes decreases with increased MWCNT content until 2 wt% since there is a tendency for MWCNT to agglomerate at 3 wt%, which causes the contact angle to increase. Enhanced thermal properties upon adding MWCNT improve the thermal stability of the membranes. The mechanical properties also improve with increased MWCNT content due to material compaction caused by intermolecular interactions. Upon analysing the performances of the PBI/MWCNT and PSF/MWCNT membranes, it is confirmed that the PBI and PBI/MWCNT membranes exhibit slightly better performances in terms of WF, RSF, R_s and S values compared to PSF and PSF/MWCNT membranes. The best overall performance for water recovery from RO reject of brackish water by FO is displayed by PBI/MWCNT_{2 wt%} compared to the other PBI and PSF membranes.

Data availability statement

Data will be made available on request.

Funding information

This research received no specific grant from funding agencies in the public, commercial, or not-for-profit sectors.

CRediT authorship contribution statement

Sharan Srinivas Venkatesh: Writing – review & editing, Writing – original draft, Visualization, Validation, Software, Resources, Methodology, Investigation, Formal analysis, Data curation, Conceptualization. **Pandiyarajan Vellaichamy:** Supervision, Project administration, Investigation, Formal analysis. **Sundararajan Thirumalachari:** Supervision, Formal analysis, Conceptualization. **Velraj Ramalingam:** Supervision, Formal analysis, Conceptualization. **Mohan Doraiswamy Raju:** Supervision, Formal analysis.

Declaration of competing interest

The authors declare that they have no known competing financial interests or personal relationships that could have appeared to influence the work reported in this paper.

Acknowledgements

The authors would like to thank Dr. Mathav Kumar (Email ID: mathav@iitm.ac.in Tel. No: +91-44-22574267), Associate Professor, Department of Civil Engineering, IIT Madras, Chennai and the staff at Chemplast Sanmar ZLD Research Laboratory, IIT Madras, Chennai for supporting this research. The authors would also like to extend their thanks to The SWRO Nemmeli Seawater Desalination Plant (P63G + G86, SH 49, Sulerikadu, Nemmeli, Vadanemmel, Tamil Nadu 603104) for the use of testing for the quality of RO reject of brackish water and DS (after the FS was transported across the membrane).

Nomenclature

Symbols

π	Osmotic Pressure
i	van't Hoff factor
C	Molar concentration of the solutes
R	Universal gas constant
T	Process Temperature
π_d	Osmotic pressure for the DS
π_f	Osmotic pressure for the FS
$\Delta\pi$	Osmotic pressure difference
ΔP	External hydraulic pressure difference
J_w	Water Flux
J_s	Reverse Solute/Salt Flux
A_m	Effective membrane area
V_0	Volume of FS at the beginning of the experiment

V_e	Volume of FS at the end of the experiment
Δt	Time interval of experiment
$C_{f,e}$	Concentration of FS at the end of the experiment
$C_{f,0}$	Concentration of FS at the beginning of the experiment
τ	Tortuosity
l	Membrane thickness
ε	Porosity
m_{wet}	Membrane wet mass
m_{dry}	Membrane dry mass
ρ_w	Water Density
ρ_p	Polymer Density
R_s	Salt rejection rate
A	Water Permeability
B	Salt Permeability
S	Structural Parameter

Abbreviations

AL-FS	Active layer facing feed solution
AL-DS	Active layer facing draw solution
DI	Deionised
DMAc	n-dimethylacetamide
DMF	n, n-dimethylformamide
DS	Draw solution
DSC	Differential scanning calorimetry
EDS	Energy dispersive X-ray spectroscopy
ECP	External concentration polarisation
FO	Forward osmosis
FS	Feed solution
FTIR	Fourier transform infrared spectroscopy
GO	Graphene oxide
ICP	Internal concentration polarisation
IP	Interfacial polymerisation
MED	Multiple-effect distillation
MSF	Multi-stage flash distillation
MWCNT	Multi-walled carbon nanotubes
NF	Nanofiltration
NIPS	Non-solvent induced phase separation
MPD	<i>m</i> -phenylenediamine
PBI	Polybenzimidazole
PI	Phase inversion
PSF	Polysulfone
PVP	Polyvinylpyrrolidone
RO	Reverse osmosis
RSF	Reverse solute flux
SEM	Scanning electron microscope
SRSF	Specific reverse solute flux
TEM	Transmission electron microscopy
TFC	Thin-film composite membranes
TFN	Thin-film nanocomposite membranes
TGA	Thermogravimetric analysis
TMC	Trimesoyl chloride
UF	Ultrafiltration
WF	Water flux
XRD	X-ray diffraction

References

- [1] K. Lutchmiah, A.R.D. Verliefe, K. Roest, L.C. Rietveld, E.R. Cornelissen, Forward osmosis for application in wastewater treatment: a review, *Water Res.* 58 (2014) 179–197, <https://doi.org/10.1016/j.watres.2014.03.045>.
- [2] W. He, Y. Dong, C. Li, X. Han, G. Liu, J. Liu, Y. Feng, Field tests of cubic-meter scale microbial electrochemical system in a municipal wastewater treatment plant, *Water Res.* 155 (2019) 372–380, <https://doi.org/10.1016/j.watres.2019.01.062>.
- [3] 2030 Water Resources Group, Charting our water future, economic frameworks to inform decision-making, 2030 Water Resources Group, 1 (2009) 1–174.
- [4] T.K. Abbas, K.T. Rashid, S. Al-Saady, A.A. Alsarayreh, A. Figoli, Q.F. AlSalhy, Decontamination of aqueous nuclear waste via pressure-driven membrane application – a short review, *Engineering and Technology Journal* 41 (9) (2023) 1152–1174, <https://doi.org/10.30684/etj.2023.140193.1454>.
- [5] Z. Shabani, M. Kahrizi, T. Mohammadi, N. Kasiri, S. Sahebi, A novel thin film composite forward osmosis membrane using bio-inspired polydopamine coated polyvinyl chloride substrate: experimental and computational fluid dynamics modelling, *Process Saf. Environ. Protect.* 47 (2021) 756–771, <https://doi.org/10.1016/j.psep.2021.01.004>.
- [6] M. Ghanbari, D. Emadzadeh, W.J. Lau, H. Riazi, D. Almasi, A.F. Ismail, Minimizing structural parameter of thin film composite forward osmosis membranes using polysulfone/halloysite nanotubes as membrane substrates, *Desalination* 377 (2016) 152–162, <https://doi.org/10.1016/j.desal.2015.09.019>.
- [7] F. Parveen, N. Hankins, Comparative performance of nanofiltration and forward osmosis membranes in a lab-scale forward osmosis membrane bioreactor, *J. Water Proc. Eng.* 28 (2018) 1–9, <https://doi.org/10.1016/j.jwpe.2018.12.003>.
- [8] R.L. McGinnis, M. Elimelech, Energy requirements of ammonia–carbon dioxide forward osmosis desalination, *Desalination* 207 (1–3) (2007) 370–382, <https://doi.org/10.1016/j.desal.2006.08.012>.
- [9] A.H. Kamel, Q.F. Alsalhy, S.S. Ibrahim, K.A. Faneer, S.A. Hashemifard, A. Jangizehi, S. Seiffert, M. Maskos, A. Shakeri, C. Bantz, Novel sodium and potassium carbon quantum dots as forward osmosis draw solutes: synthesis, characterization and performance testing, *Desalination* 567 (2023) 116956, <https://doi.org/10.1016/j.desal.2023.116956>.
- [10] M. Yan, M. Shao, J. Li, N. Jiang, Y. Hu, W. Zeng, M. Huang, Antifouling forward osmosis membranes by ϵ -polylysine mediated molecular grafting for printing and dyeing wastewater: preparation, characterization, and performance, *J. Membr. Sci.* 668 (2023) 121288, <https://doi.org/10.1016/j.memsci.2022.121288>.
- [11] N. Akther, A. Sodiq, A. Giwa, S. Daer, H.A. Arafat, S.W. Hasan, Recent advancements in forward osmosis desalination: a review, *Chem. Eng. J.* 281 (2015) 502–522, <https://doi.org/10.1016/j.cej.2015.05.080>.
- [12] X. Liu, H.Y. Ng, Fabrication of layered silica–polysulfone mixed matrix substrate membrane for enhancing performance of thin-film composite forward osmosis membrane, *J. Membr. Sci.* 481 (2015) 148–163, <https://doi.org/10.1016/j.memsci.2015.02.012>.
- [13] A. Haupt, A. Lerch, Forward osmosis application in manufacturing industries: a short review, *Nat. Commun.* 8 (3) (2018) 1–9, <https://doi.org/10.3390/membranes8030047>.
- [14] D.J. Johnson, W.A. Suwaileh, A.W. Mohammed, N. Hilal, Osmotic’s potential: an overview of draw solutes for forward osmosis, *Desalination* 434 (2017) 100–120, <https://doi.org/10.1016/j.desal.2017.09.017>.
- [15] S.C. Chen, X.Z. Fu, T.S. Chung, Fouling behaviors of polybenzimidazole (PBI)–polyhedral oligomeric silsesquioxane (POSS)/polyacrylonitrile (PAN) hollow fiber membranes for engineering osmosis processes, *Desalination* 335 (1) (2014) 17–26, <https://doi.org/10.1016/j.desal.2013.12.005>.
- [16] S. Morales-Torres, C.M. Esteves, J.L. Figueiredo, A.M. Silva, Thin-film composite forward osmosis membranes based on polysulfone supports blended with nanostructured carbon materials, *J. Membr. Sci.* 520 (2016) 326–336, <https://doi.org/10.1016/j.memsci.2016.07.009>.
- [17] N. Akther, S. Daer, Q. Wei, I. Janajreh, S.W. Hasan, Synthesis of polybenzimidazole (PBI) forward osmosis (FO) membrane and computational fluid dynamics (CFD) modeling of concentration gradient across membrane surface, *Desalination* 452 (2019) 17–28, <https://doi.org/10.1016/j.desal.2018.11.003>.
- [18] W.A. Suwaileh, D.J. Johnson, S. Sarp, N. Hilal, Advances in forward osmosis membranes: altering the sub-layer structure via recent fabrication and chemical modification approaches, *Desalination* 436 (2018) 176–201, <https://doi.org/10.1016/j.desal.2018.01.035>.
- [19] M.H. Salih, A.F. Al-Alawy, MgCl₂ and MgSO₄ as draw agents in forward osmosis process for East Baghdad oilfield produced water treatment, *Desalination Water Treat.* 256 (2022) 80–88, <https://doi.org/10.5004/dwt.2022.28408>.
- [20] J.N. Krishnan, K.R. Venkatachalam, O. Ghosh, K. Jhaveri, A. Palakodeti, N. Nair, Review of thin film nanocomposite membranes and their applications in desalination, *Front. Chem.* 10 (2022) 781372, <https://doi.org/10.3389/fchem.2022.781372>.
- [21] J.R. McCutcheon, M. Elimelech, Influence of concentrative and dilutive internal concentration polarization on flux behavior in forward osmosis, *J. Membr. Sci.* 284 (1–2) (2006) 237–247, <https://doi.org/10.1016/j.memsci.2006.07.049>.
- [22] J.R. McCutcheon, M. Elimelech, Modeling water flux in forward osmosis: implications for improved membrane design, *AIChE J.* 53 (7) (2007) 1736–1744, <https://doi.org/10.1002/aic.11197>.
- [23] M. Arjmandi, M. Peyravi, A. Altaee, A. Arjmandi, M.P. Chenar, M. Jahanshahi, E. Binaeian, A state-of-the-art protocol to minimize the internal concentration polarization in forward osmosis membranes, *Desalination* 480 (2020) 114355, <https://doi.org/10.1016/j.desal.2020.114355>.
- [24] S. Sahebi, S. Phuntsho, Y.C. Woo, M.J. Park, L.D. Tijing, S. Hong, H.K. Shon, Effect of sulfonated polyethersulfone substrate for thin film composite forward osmosis membrane, *Desalination* 389 (2016) 129–136, <https://doi.org/10.1016/j.desal.2015.11.028>.
- [25] H. Jain, M.C. Garg, Fabrication of polymeric nanocomposite forward osmosis membranes for water desalination – a review, *Environ. Technol. Innovat.* 23 (2021) 1–27, <https://doi.org/10.1016/j.eti.2021.101561>.
- [26] I. Tavakol, S. Hadadpour, Z. Shabani, M.A. Tofighy, T. Mohammadi, S. Sahebi, Synthesis of novel thin film composite (TFC) forward osmosis (FO) membranes incorporated with carboxylated carbon nanofibers (CNFs), *J. Environ. Chem. Eng.* 8 (2020) 104614, <https://doi.org/10.1016/j.jece.2020.104614>.
- [27] D. Emadzadeh, W.J. Lau, T. Matsuura, A.F. Ismail, M. Rahbari-Sisakht, Synthesis and characterization of thin film nanocomposite forward osmosis membrane with hydrophilic nanocomposite support to reduce internal concentration polarization, *J. Membr. Sci.* 449 (2014) 74–85, <https://doi.org/10.1016/j.memsci.2013.08.014>.
- [28] M.J. Park, S. Phuntsho, T. He, G.M. Nisola, L.D. Tijing, X.-M. Li, G. Chen, W.-J. Chung, H.K. Shon, Graphene oxide incorporated polysulfone substrate for the fabrication of flat-sheet thin-film composite forward osmosis membranes, *J. Membr. Sci.* 493 (2015) 496–507, <https://doi.org/10.1016/j.memsci.2015.06.053>.
- [29] M. Amini, M. Jahanshahi A. Rahimpour, Synthesis of novel thin film nanocomposite (TFN) forward osmosis membranes using functionalized multi-walled carbon nanotubes, *J. Membr. Sci.* 435 (2013) 223–241, <https://doi.org/10.1016/j.memsci.2013.01.041>.
- [30] R.R. Darabi, M. Jahanshahi, M. Peyravi, A support assisted by photocatalytic Fe₃O₄/ZnO nanocomposite for thin-film forward osmosis membrane, *Chem. Eng. Res. Des.* 133 (2018) 11–25, <https://doi.org/10.1016/j.cherd.2018.02.029>.
- [31] J. Jang, I. Park, S.-S. Chee, J.-H. Song, Y. Kang, C. Lee, W. Lee, M.-H. Ham, I.S. Kim, Graphene oxide nanocomposite membrane cooperatively cross-linked by monomer and polymer overcoming the trade-off between flux and rejection in forward osmosis, *J. Membr. Sci.* 598 (2019) 117684, <https://doi.org/10.1016/j.memsci.2019.117684>.
- [32] S. Li, Y. Li, Y. Shao, H. Wang, Emerging two-dimensional materials constructed nanofluidic fiber: properties, preparation and applications, *Advanced Fiber Materials* 4 (2022) 129–144, <https://doi.org/10.1007/s42765-021-00111-w>.
- [33] P. Wagh, X. Zhang, R. Blood, P.M. Kekenus-Huskey, P. Rajapaksha, Y. Wei, I.C. Escobar, Increasing salt rejection of polybenzimidazole nanofiltration membranes via the addition of immobilized and aligned aquaporins, *Processes* 7 (2) (2019) 76, <https://doi.org/10.3390/pr7020076>.
- [34] M.F. Flanagan, I.C. Escobar, Novel charged and hydrophilized polybenzimidazole (PBI) membranes for forward osmosis, *J. Membr. Sci.* 434 (2013) 85–92, <https://doi.org/10.1016/j.memsci.2013.01.039>.
- [35] S. Zhao, L. Zou, D. Mulcahy, Brackish water desalination by a hybrid forward osmosis–nanofiltration system using divalent draw solute, *Desalination* 284 (2012) 175–181, <https://doi.org/10.1016/j.desal.2011.08.053>.
- [36] A. Altaee, N. Hilal, High recovery rate NF–FO–RO hybrid system for inland brackish water treatment, *Desalination* 363 (2015) 19–25, <https://doi.org/10.1016/j.desal.2014.12.017>.
- [37] N.K. Khanzada, J.S. Khan, P.A. Davies, Performance evaluation of reverse osmosis (RO) pre-treatment technologies for in-land brackish water treatment, *Desalination* 406 (2017) 44–50, <https://doi.org/10.1016/j.desal.2016.06.030>.

- [38] Y. Yuan, F. Johnson, I. Cabasso, Polybenzimidazole (PBI) molecular weight and Mark-Houwink equation, *J. Appl. Polym. Sci.* 112 (6) (2009) 3436–3441, <https://doi.org/10.1002/app.29817>.
- [39] G. Dahe, R.P. Singh, K.W. Dudeck, D. Yang, K.A. Berchtold, Influence of non-solvent chemistry on polybenzimidazole hollow fiber membrane preparation, *J. Membr. Sci.* 577 (2019) 91–103, <https://doi.org/10.1016/j.memsci.2019.02.001>.
- [40] A.O. Rashed, A.M. Esawi, A.R. Ramadan, Novel polysulfone/carbon nanotube-polyamide thin film nanocomposite membranes with improved water flux for forward osmosis desalination, *ACS Omega* 5 (24) (2020) 14427–14436, <https://doi.org/10.1021/acsomega.0c00973>.
- [41] R.P. Singh, G.J. Dahe, K.W. Dudeck, K.A. Berchtold, Macrovoid-free high performance polybenzimidazole hollow fiber membranes for elevated temperature H₂/CO₂ separations, *Int. J. Hydrogen Energy* 45 (51) (2020) 27331–27345, <https://doi.org/10.1016/j.ijhydene.2020.07.091>.
- [42] J.F. Sark, N. Jullok, W.J. Lau, Improving the structural parameter of the membrane sublayer for enhanced forward osmosis, *Membranes* 448 (11) (2021) 1–18, <https://doi.org/10.3390/membranes11060448>.
- [43] T.Y. Cath, A.E. Childress, M. Elimelech, Forward osmosis: principles, applications, and recent developments, *J. Membr. Sci.* 281 (1–2) (2006) 70–87, <https://doi.org/10.1016/j.memsci.2006.05.048>.
- [44] J. Korenak, S. Basu, M. Balakrishnan, C. Helix-Nielsen, I. Petrinic, Forward osmosis in wastewater treatment processes, *Acta Chim. Slov.* 64 (1) (2017) 83–94, <https://doi.org/10.17344/acsi.2016.2852>.
- [45] F.H. Akhtar, M. Kumar, L.F. Villalobos, H. Vovusha, R. Shevate, U. Schwingenschlogl, K.-V. Peinemann, Polybenzimidazole-based mixed membranes with exceptional high water vapor permeability and selectivity, *J. Mater. Chem. A* 5 (2017) 21807–21819, <https://doi.org/10.1039/C7TA05081J>.
- [46] K.Y. Wang, M. Weber, T.S. Chung, Polybenzimidazoles (PBIs) and state-of-the-art PBI hollow fiber membranes for water, organic solvent and gas separations: a review, *J. Mater. Chem. A* 10 (2022) 8687–8718, <https://doi.org/10.1039/D2TA00422D>.
- [47] J. Park, Y.G. Jeong, Investigation of microstructure and electric heating behavior of hybrid polymer composite films based on thermally stable polybenzimidazole and multiwalled carbon nanotube, *Polymer* 59 (2015) 102–109, <https://doi.org/10.1016/j.polymer.2015.01.003>.
- [48] W.-Y. Wang, J.-Y. Shi, J.-L. Wang, Y.-L. Li, N.-N. Gao, Z.-X. Liu, W.-T. Lian, Preparation and characterization of PEG-gMWCNTs/PSf nano-hybrid membranes with hydrophilicity and antifouling properties, *Royal Society of Chemistry* 5 (2015) 84746, <https://doi.org/10.1039/C5RA16077D>.
- [49] S. Daer, N. Akther, Q. Wei, H.K. Shon, S.W. Hasan, Influence of silica nanoparticles on the desalination performance of forward osmosis polybenzimidazole membranes, *Desalination* 491 (2020) 114441, <https://doi.org/10.1016/j.desal.2020.114441>.
- [50] A.A. Shah, Y.H. Cho, H. Choi, S.-E. Nam, J.F. Kim, Y. Kim, Y.-I. Park, H. Park, Facile integration of halloysite nanotubes with bioadhesive as highly permeable interlayer in forward osmosis membranes, *J. Ind. Eng. Chem.* 73 (2019) 276–285, <https://doi.org/10.1016/j.jiec.2019.01.039>.
- [51] Suryani, C.-M. Chang, Y.-L. Liu, Y.M. Lee, Polybenzimidazole membranes modified with polyelectrolyte-functionalized multiwalled carbon nanotubes for proton exchange membrane fuel cells, *J. Mater. Chem.* 21 (20) (2011) 7480–7486, <https://doi.org/10.1039/C1JM10439J>.
- [52] V. Datsyuk, T. Svitlana, R. Stephanie, Carbon-nanotube–polymer nanofibers with high thermal conductivity, *Carbon* 52 (2013) 617–620, <https://doi.org/10.1016/j.carbon.2012.09.045>.
- [53] N. Koutahzadeh, M.R. Esfahani, P.E. Arce, Sequential use of UV/H₂O₂—(PSF/TiO₂/MWCNT) mixed matrix membranes for dye removal in water purification: membrane permeation, fouling, rejection, and decolorization, *Environ. Eng. Sci.* 33 (6) (2016) 430–440, <https://doi.org/10.1089/ees.2016.0023>.
- [54] R.R.R. Sulaiman, R. Walvekar, W.Y. Wong, M. Khalid, M.M. Pang, Proton conductivity enhancement at high temperature on polybenzimidazole membrane electrolyte with acid-functionalized graphene oxide fillers, *Membranes* 344 (12) (2022) 1–23, <https://doi.org/10.3390/membranes12030344>.
- [55] A. Muhulet, C. Tuncel, F. Miculescu, A.M. Pandele, C. Bobirica, C. Orbeci, L. Bobirica, A. Palla-Papavlu, S.I. Voicu, Synthesis and characterization of polysulfone–TiO₂ decorated MWCNT composite membranes by sonochemical method, *Appl. Phys. A* 126 (233) (2020) 1–9, <https://doi.org/10.1007/s00339-020-3408-9>.
- [56] A. Jean-Fulcrand, M.A. Masen, T. Bremner, J.S.S. Wong, High temperature tribological properties of polybenzimidazole (PBI), *Polymer* 128 (2017) 159–168, <https://doi.org/10.1016/j.polymer.2017.09.026>.
- [57] A.B. Bocarsly, E.V. Niangar, Fuel cells – PROTON-EXCHANGE MEMBRANE FUEL CELLS | membranes: elevated temperature, *Encyclopaedia of Electrochemical Power Sources* (2009) 724–733, <https://doi.org/10.1016/B978-044452745-5.00232-X>.
- [58] S.M. Momeni, M. Pakizeh, Preparation, characterization and gas permeation study of PSf/MgO nanocomposite membrane, *Braz. J. Chem. Eng.* 30 (3) (2013) 589–597, <https://doi.org/10.1590/S0104-66322013000300016>.
- [59] J.B. Rose, Preparation and properties of poly(arylene ether sulphones), *Polymer* 15 (7) (1974) 456–465, [https://doi.org/10.1016/0032-3861\(74\)90111-6](https://doi.org/10.1016/0032-3861(74)90111-6).
- [60] D. Emadzadeh, W.J. Lau, T. Matsuura, M. Rahbari-Sisakht, A.F. Ismail, A novel thin film composite forward osmosis membrane prepared from PSf–TiO₂ nanocomposite substrate for water desalination, *Chem. Eng. J.* 237 (2014) 70–80, <https://doi.org/10.1016/j.cej.2013.09.081>.